Role of Capillary Stresses in Film Formation

Mahesh S. Tirumkudulu* and William B. Russel

Department of Chemical Engineering, Princeton University, Princeton, New Jersey 08544

Received September 1, 2003. In Final Form: December 29, 2003

Stresses generated during film formation were deduced from the deflection of a copper cantilever coated with a drying latex. Experiments with particles of varying radii and glass transition temperatures (T_g) focused on conditions for which capillary stresses normal to the film deform the particles to close the voids. Soft particles (low T_g) formed continuous films, but hard ones (high T_g) produced fascinating arrays of cracks. For both soft and rigid particles, the lateral stresses were tensile and scaled on the surface tension divided by the particle radius. Clearly, tensile stresses in the plane of the film responsible for cracking arise from the same capillary pressure that drives compression in the normal direction. Solving the model (Routh & Russel 1996, 1999) for lateral flow of the fluid dispersion prior to close packing and deformation of the solid beyond close packing yields volume fraction, film thickness, and stress profiles for comparison with observations for both film-forming and film-cracking cases.

1. Introduction

When a thin film of latex containing soft polymer particles is applied on a nonporous surface, the evaporation of the solvent (in this case, water) concentrates the particles into a closed packed array. Further evaporation is accompanied by stresses in the wet film that deform the particles so as to close the pores. The contact between the particles allows the polymer chains to diffuse across the particle−particle interface to fuse the particles which ultimately results in a homogeneous film that is free of voids. Although the three stages of film formation, i.e., drying, deformation, and coalescence, have been studied for a long time, the mechanisms responsible for drying and particle deformation are rather complex and not fully articulated.

The various aspects of the drying process in film formation have recently been reviewed by Holl et al.[1] who distinguish three primary types or modes of drying in a wet film. The first mode, which is rarely observed, corresponds to the homogeneous drying where the water concentration is spatially homogeneous in the film and all parts of the film dry at the same rate. The second mode of drying occurs under conditions of negligible particle diffusivity when the evaporating liquid concentrates the particles at the liquid−air interface resulting in a "sheet" of packed particles at the surface of the film. The packed region grows in thickness as the vertical convection induced by the capillary pressure draws more particles into the region. Note that the capillary pressure is caused by the liquid menisci formed between the particles at the top of the packed region. Finally, the third mode involving lateral front propagation occurs when the nonuniform thickness of the film (thinnest at the film edge) causes the particles to concentrate first at the edges (Figure 1). Here, in contrast to the previous case, the low pressure caused by the liquid menisci at the edge draws the dispersion from the bulk, resulting in a lateral front propagation.

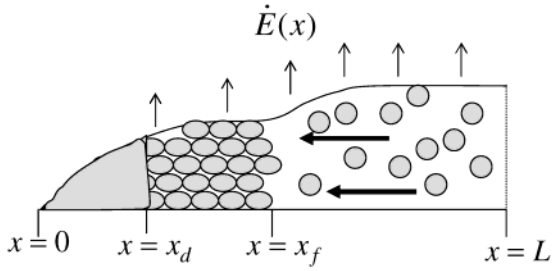

Figure 1. A schematic diagram of a latex film drying containing the clear film region ($0 < x < x_d$), saturated solid region ($x_d < x < x_f$), and fluid region ($x_f < x < L$).

Routh and Russel[2] have modeled the drying of a wet film with rigid (nondeforming particles) while accounting for the capillary pressure that results in lateral propagation of the front. While the vertical front occurs when the vertical convection dominates diffusion, propagation of a front laterally is observed when particle diffusion is large enough to maintain a homogeneous particle concentration in the vertical direction. Sutanto et al.[3] have recently demonstrated the presence of both types of fronts by examining the particle distribution in latex films containing polystyrene and poly(butyl methacrylate) spheres using cryogenic scanning electron microscopy. An alternate explanation for the lateral flow was given by Deegan et al.[4] who suggested that a pinned liquid−solid contact line at the edges along with a spatially varying evaporation rate would induce bulk flow to the edges; here the flow results from the need to maintain the film profile dictated by surface tension.

The second step in the film formation process involves deformation of individual particles. The earliest theory, proposed by Hertz,[5] considered elastic deformation of two touching spheres pushed together by external point forces

* Current address: Department of Chemical Engineering, Indian Institute of Technology−Bombay, Mumbai 400076, India. E-mail: mahesh@che.iitb.ac.in.

(1) Holl, Y.; Keddie, J. L.; McDonald, P. J.; Winnik, W. A. *Film formation in coatings: Mechanisms, Properties and Morphology*; Provder, T., Urban, M. W., Eds.; ACS Symposium Series 790; American Chemical Society: Washington, DC, 2001; Chapter 1, pp 2−26.

(2) Routh, A. F.; Russel, W. B. Horizontal drying fronts during solvent evaporation from latex films. *AIChE J.* **1998**, *44* (9), 2088−2098.

(3) Sutanto, E.; Ma, Y. H.; Davis, T.; Scriven, L. E. *Film formation in coatings: Mechanisms, Properties and Morphology*; ACS Symposium Series 790; American Chemical Society: Washington, DC, 2001; Chapter 10, pp 174−192.

(4) Deegan, R. D.; Bakajin, O.; Dupont, T. F.; Huber, G.; Nagel, S. R.; Witten, T. A. Capillary flow as the cause of ring stains from dried liquid drops. *Nature* **1997**, *389*, 827−829.

(5) Maugis, D. *Contact, Adhesion and Rupture of Elastic Solids*; Springer: Berlin, 1999.

10.1021/la0356250 CCC: $27.50
Published on Web 02/25/2004

(F) acting along the line joining their centers and arrived at the following expression for the local strain

$$\epsilon_R = (3F/16GR_o^2)^{2/3}$$

with G the shear modulus, R_o the original radius of the particles, and ϵ_R defined as the ratio of the change in the center to center distance to the initial distance before deformation. In contrast, the viscous sintering of two spheres, proposed by Frenkel,[6] balances the interfacial tension (γ), which minimizes the particle surface area, with the viscous forces resisting deformation to relate local strain to particle viscosity (μ_p) and time t as

$$\epsilon_R = \gamma t/2\mu_p R_o$$

Finally, a balance between the surface energy of the elastic spheres and elastic deformation energy for a pair of force free particle gives[7]

$$\epsilon_R = 0.234(\gamma/GR_o)^{2/3}$$

While the above-mentioned models relate the external force to the local deformation, four distinct film formation regimes have been identified on the basis of the nature of external forces causing deformation. *Wet sintering* is said to occur when the interfacial tension between the particles and the surrounding solvent drives the particle deformation.[8] Similarly, *dry sintering* is caused by the interfacial tension between the particles and surrounding air and occurs after all the solvent has evaporated. Brown,[9] on the other hand, proposed the driving force to be the capillary pressure that results from the presence of liquid menisci of negative curvature between closely packed particles (*capillary deformation*). In contrast to the previously mentioned models, Sheetz[10] accounted for inhomogeneous drying by proposing a vertical drying front of particles that were deformed by capillary forces (*Sheetz deformation*). Although experimental evidence in support of all the above regimes was available, a complete understanding of the conditions responsible for each regime was missing. To this end Routh and Russel,[11] henceforth referred to as RR, considered the viscoelastic deformation of a pair of particles due to both interfacial tension and external forces exerted by contacting neighbors. Starting from a microscopic description of the local stress versus strain relation, they volume averaged over all possible orientations of the pair to arrive at a macroscopic description of stress and strain for a deforming film. On the basis of this model they showed that for typical evaporation rates, a single dimensionless group, λ, obtained by comparing the viscous deformation and evaporation rates could distinguish between the various regimes of film formation. While very low values of λ lead to wet sintering, a large value of λ signifies dry sintering. Intermediate values coupled with homogeneous drying lead to capillary compression. However, in the presence of a vertical drying front, intermediate values of λ result in *Sheetz deformation*. A comparison of the model predictions with experimental results shows good qualitative agreement.[12]

Table 1. Details of the Dispersions Used for Experiments

dispersion	particle composition	particle diameter (nm)	T_g (°C)	film forming temperature (°C)
WCFA	BA/MMA/AA	290	22	16
PPG342	PS	342	100	
GMA610	PS core, PMMA/GMA shell	610	65−80	

In this study, we monitor the transverse stress development in a film of a drying latex cast on a thin copper substrate by measuring the deflection of the underlying substrate. The drying process results in an evaporation flux that not only varies spatially across the film but also results in a laterally propagating drying front. Thus the measured substrate deflection, which is a measure of the average transverse stress in the film and depends on the particle rheology and film dimensions, is also a strong function of the exact location of the drying front.[13,14] Our objective is to solve the RR model while accounting for the lateral inhomogeneities and compare the predicted average stress and front position with the measured values for dispersions containing particles of varying radii and glass transition temperatures. After a brief description of the experimental setup, we present in section 3 the governing equations for the drying and film formation processes along with a detailed account of the numerical procedure involved in solving the equations. Finally, in section 4, the results of the experiments are compared to those predicted by theory.

2. Experiments

Experiments were performed with three different aqueous dispersions that contained, as the dispersed phase, polymer spheres of varying radii and glass transition temperatures. The film-forming dispersion, henceforth referred to as WCFA, contained spheres of diameter 290 nm that deformed completely upon drying (under ambient conditions) to yield transparent homogeneous films. While the glass transition temperature was measured as 22 °C, the manufacturers (Rohm and Haas Company) specify the minimum film-forming temperature as 16 °C. The original dispersion was centrifuged and the supernatant replaced by deionized water, resulting in a high dispersion viscosity at relatively low solids loading. The remaining two non-film-forming dispersions, namely, PPG342 and GMA610, contained particles of mean diameter 342 and 610 nm, respectively. Here, due to the relatively high glass transition temperature, the dispersions resulted in films that were opaque and in most cases contained large cracks. The properties of all the three dispersions are detailed in Table 1.

The stress generated in a thin film during drying can be measured according to the classical cantilever tech-

(6) Frenkel, J. Viscous flow of crystalline bodies under the action of surface tension. *J. Phys.* 1945, *9*(5), 385−391.

(7) Johnson, K. L.; Kendall, K.; Roberts, A. D. Surface energy and the contact of elastic solids. *Proc. R. Soc. London, Ser. A* **1971**, *324*, 301−313.

(8) Vanderhoff, J. W.; Tarkowski, H. L.; Jenkins, M. C.; Bradford, E. B. Theoretical consideration of the interfacial forces involved in the coalescence of latex particles. *J. Macromol. Chem.* **1966**, *1* (2), 361−397.

(9) Brown, G. L. Formation of films from polymer dispersions. *J. Polym. Sci.* **1956**, *22*, 423−434.

(10) Sheetz, D. P. Formation of films by drying of latex. *J. Appl. Polym. Sci.* 1965, *9*, 3759−3773.

(11) Routh, A. F.; Russel, W. B. A process model for latex film formation: Limiting regimes for individual driving forces. *Langmuir* **1999**, *15* (22), 7762−7773.

(12) Routh, A. F.; Russel, W. B. Deformation mechanisms during latex film formation: Experimental evidence. *Ind. Eng. Chem. Res.* **2001**, *40* (20), 4302−4308.

(13) Chiu, R. C.; Cima, M. J. Drying of granular ceramic films: II drying stress and saturation uniformity. *J. Am. Ceram. Soc.* **1993**, *76* (11), 2769−2777.

(14) Martinez, C. J.; Lewis, J. A. Shape evolution and stress development during latex-silica film formation. *Langmuir* **2002**, *18* (12), 4689−4698.

nique[15,16] from the deflection of the underlying elastic substrate. Since our experimental setup is quite similar to that employed by Petersen et al.,[17] only a brief description will be given here. Thin films of dispersions were applied on rectangular strips of copper of mean thickness 76 μm and Young's modulus, 117 GPa. One end of the freely suspended substrate was clamped while a small mirror (mylar) was glued to the other (free) end. A laser beam incident on the mirror was collected, on reflection, by a position detector. Care was taken to ensure that the reflected beam was perpendicular to the detector surface. The signals from the detector were acquired at intervals of 0.1 s by a computer. In addition, a sensor placed in the vicinity of the drying film provided temperature and relative humidity data to the computer. The entire setup was enclosed in a Plexiglas chamber to prevent air circulation from affecting the experiments. The experiments were conducted over a range of temperatures (19−24 °C) and relative humidities (30−70%). Evaporation rates were determined separately, under the same ambient conditions, by recording the weight of the drying film as a function of time.

The transverse stress in the film can be determined from the well-known plate/beam deflection relation[17]

$$\sigma = \frac{E_s t_s^{\,3}}{6 t_f (t_s + t_f)} \frac{\theta}{l_f} \qquad (1)$$

where σ, the transverse stress in the plane of the film, is assumed to be constant throughout the film. Also, E_s and t_s are, respectively, the Young's modulus and thickness of the substrate, θ is the deflection angle measured at the tip of the film, and t_f and l_f are, respectively, the average thickness and length of the drying film. In the derivation of eq 1, the substrate curvature is assumed to be constant along its length. In the case of inhomogeneous drying where a front propagates horizontally and particle deformation is confined to the packed particle region, the curvature will vary spatially. For the purposes of comparison with the model predictions, however, we integrate the predicted (spatially varying) transverse stress along the length of the film to arrive at an average transverse stress that is equivalent to the measured stress (1). Further, the film is assumed to be well bonded to the substrate so that any slip at the film−substrate interface is ignored. Finally, Corcoran[15] shows that the substrate deflection does not affect the film stress as long as the ratio of either the substrate to the film thickness or the film to the substrate modulus is very small, as in our situation.

The measured deflection angle, in our experiments, is corrected for the evaporation of the solvent and the corresponding change in the average height of the film so as to yield the bulk stress induced by film formation/particle deformation.

3. Model and Computations

Figure 1 shows schematically the drying of a latex film. When the particle diffusion is large compared to the convection in the direction perpendicular to the plane of the film, the nonuniform thickness of the film (thinnest at the edge) causes the particles to concentrate first at the edges (Figure 1). The low pressure caused by the liquid menisci at the edge draws the dispersion from the bulk, resulting in a front that propagates laterally. This results in the formation of two domains, namely, an outer saturated "solid" domain where the particle concentration is either greater than or equal to that for random close packing and an inner "fluid" domain containing the dilute dispersion (Figure 2). Since the capillary stresses are the largest at the outer edge of the solid domain, a second front separating a region containing completely deformed particles (clear film region) and saturated solid domain is seen in the case of film-forming latices. However, in the non-film-forming case (i.e., rigid particles), the liquid menisci recede from the edge of the film resulting in a second front that separates the dry solid from the saturated solid.

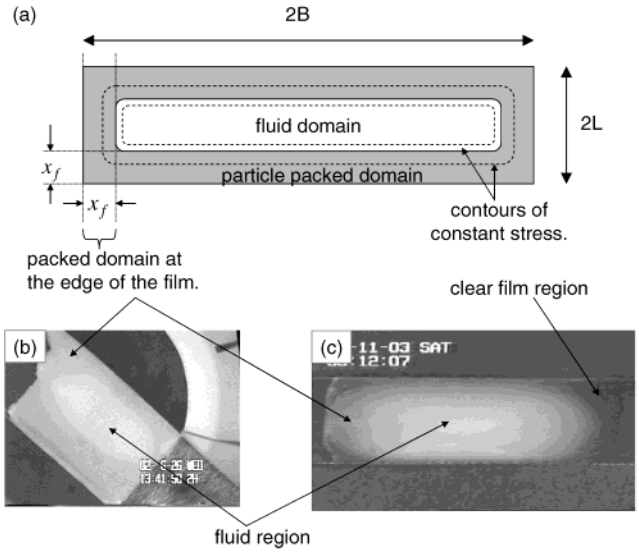

Figure 2. (a) A schematic diagram of a latex film drying on a substrate showing the two-dimensional propagation of the drying front. The central region contains the dilute dispersion (fluid domain) whereas the outer gray region refers to the solid domain. The front position is given by x_f while the contours of constant stress are shown by the dashed lines. (b) A thin film of a non-film-forming dispersion (PPG342, see Table 1) shows the presence of saturated solid and fluid regions. (c) A thin film of a film-forming dispersion (WCFA, see Table 1) shows the presence of clear film, saturated, and fluid regions.

RR modeled the deformation of the particles in the saturated solid by considering the viscoelastic deformation of a pair of particles in the shape of truncated spheres to relate the external force (F) due to contacting neighbors to the particle strain ϵ_R.

$$\frac{F}{\pi R_o^{\,2}}\left[1 - \frac{1}{2}\epsilon_R + \frac{1}{8}\epsilon_R^{\,2}\right] = \int_0^t G(t-t')\frac{d\epsilon_R^{\,2}}{dt}\,dt' + O(\epsilon_R^{\,3}) \qquad (2)$$

where $G(t - t')$ is the stress relaxation modulus of the particles. According to the sign convention adopted by RR, $\epsilon_R > 0$ represents compression. The macroscopic stress and strain relation is obtained by volume averaging the force dipoles induced in each pair of particles over all possible orientations and adding the contribution from the capillary pressure in the water P_c as

(15) Corcoran, E. M. Determining stresses in organic coatings using plate beam method. *J. Paint Technol.* **1969**, *41* (538), 635−640.
(16) Perera, D. Y.; Eynde, D. V. Considerations on a cantilever (beam) method for measuring the internal stress in organic coatings. *J. Coating Technol.* **1981**, *53* (677), 39−44.
(17) Petersen, C.; Heldmann, C.; Johannsmann, D. Internal stresses during film formation of polymer latices. *Langmuir* **1999**, *15*, 7745−7751.

$$\sigma_{ij} = -\delta_{ij}\left\{P_c - \frac{\nu\phi_{rcp}}{140}\int_0^t G(t-t')\frac{d}{dt'}(\epsilon_{mm}{}^2 + 2\epsilon_{mn}\epsilon_{nm})\,dt'\right\} + \frac{\nu\phi_{rcp}}{35}\int_0^t G(t-t')\frac{d}{dt'}(\epsilon_{mm}\epsilon_{ij} + 2\epsilon_{im}\epsilon_{mj})\,dt' \quad (3)$$

Here ϵ_{ij} is the macroscopic strain tensor, ϕ_{rcp} is the random close packing concentration, and ν is the number of contacting neighbors. Note that the above stress expression is a corrected form of that appearing in RR with the contribution from the particle−solvent surface tension neglected.

If 3 is the direction perpendicular to the surface of the film, we must have $\sigma_{33} = 0$. By restricting the analysis to one-dimensional compaction where the strain is given by $\epsilon_{ij} = \epsilon\delta_{i3}\delta_{j3}$, the bulk stress simplifies to

$$\sigma_{ij} = -\delta_{ij}\left[P_c + \frac{\nu\phi_{rcp}}{140}\int_0^t G(t-t')\frac{d\epsilon^2}{dt'}\,dt'\right] - \delta_{i3}\delta_{j3}\frac{\nu\phi_{rcp}}{35}\int_0^t G(t-t')\frac{d\epsilon^2}{dt'}\,dt' \quad (4)$$

Note that the bulk strain is related to the particle concentration via the overall conservation expression, $\phi = \phi_{rcp}/(1-\epsilon)$. For the case of elastic particles, where the relaxation modulus is simply G, we obtain the capillary pressure as

$$P_c = -\frac{3\nu\phi_{rcp}G}{28}\left(1 - \frac{\phi_{rcp}}{\phi}\right)^2 \quad (5)$$

Similarly, for viscous particles where $G(t-t') \equiv \mu_p\delta(t-t')$, the capillary pressure is given by

$$P_c = -\frac{3\nu\phi_{rcp}\mu_p}{14}\left(1 - \frac{\phi_{rcp}}{\phi}\right)\frac{\phi_{rcp}}{\phi^2}\frac{d\phi}{dt} \quad (6)$$

Thus, increasing the particle concentration increases the magnitude of the (negative) capillary pressure and consequently effects the transverse stresses (4).

If the particle concentration were to remain spatially homogeneous throughout the drying process, the aforementioned relations (4−6) would be sufficient to describe the stress development as a function of time. In the case of inhomogeneous drying with a front propagating horizontally, however, the particle deformation in the packed bed is coupled to the flow in the fluid region, so the dynamics of both domains need to be considered (Figure 1). On the fluid side, the governing equation for the height, h, is obtained from a lubrication analysis[2] that balances the surface-tension-driven flow resulting from the gradient of the film curvature against the viscous stresses

$$\frac{\partial h}{\partial t} + \frac{\gamma_d}{3\mu_d}\frac{\partial}{\partial x}\left(h^3\frac{\partial^3 h}{\partial x^3}\right) = -\dot{E}(x) \quad (7)$$

where $\dot{E}(x)$ is the spatially varying evaporation rate and μ_d and γ_d are, respectively, the viscosity and the surface tension of the dispersion, assumed to be spatially uniform and independent of time. Note that, in the absence of the surface tension term, the height of the film will decrease at a rate set by evaporation. As mentioned previously, the low suction pressure caused by the liquid menisci between particles at the edge of the film draws liquid from the fluid region into the solid domain. Consequently, eq 7 suggests that the fluid domain satisfies the required flux by altering its curvature to set the requisite pressure gradient across the fluid domain.

If the particle diffusion maintains a uniform particle concentration in the vertical direction while the fluid convection dominates the spanwise direction, the particle conservation equation simplifies to

$$\frac{\partial h\phi}{\partial t} + \frac{\gamma_d}{3\mu_d}\frac{\partial}{\partial x}\left(\phi h^3\frac{\partial^3 h}{\partial x^3}\right) = 0 \quad (8)$$

In the packed region, the flow is described by Darcy's law relating the solvent velocity in the porous medium to the gradient of applied pressure. In the present case, the pressure gradient results from the spatially varying capillary pressure so that

$$u_x(1-\phi) = -k_p(\phi)\frac{\partial P_c}{\partial x}$$
$$k_p(\phi) = \frac{2R_o{}^2(1-\phi)^3}{75\phi^2} \quad (9)$$

where $k_p(\phi)$ is the permeability of the packed domain and P_c is determined by the constitutive relations in eqs 5 and 6. The solvent material balance across the packed domain relates the height and particle concentration to the evaporation rate and gradient of the capillary pressure

$$\frac{\partial}{\partial t}(h(1-\phi)) = -\dot{E}(x) + \frac{\partial}{\partial x}(hu_x(1-\phi)) \quad (10)$$

where u_x is given by (9). Since the particles in the packed domain are compacted and not convected, the particle conservation equation is simply

$$\frac{d}{dt}(h\phi) = 0 \quad (11)$$

These equations depend on the capillary length $h_o(\gamma_d/(\mu_d\dot{E}_o))^{1/4}$ and the lateral dimension of the closed-packed (or saturated) solid region of the film being large compared to the film thickness. The former justifies the lubrication approximation leading to (7), (8), and (10). The latter allows us to neglect the regions just inside the edges where shear stresses prevent the film from contracting laterally, accomplishing the transition from the stress-free edge to the interior in which the plane strain approximation inherent in eqs 4 and 11 is valid.

For the purposes of numerical computation, the governing equations for both domains were simplified by introducing new variables. Nondimensionalizing the spatial coordinate with the half length of the film, L, the height with the initial average height, h_o, and time with the total evaporation rate ($h_o/\dot{E}_o$) converts the governing equations for the solid domain into

$$\frac{\partial}{\partial \bar{t}}(\bar{h}(1-\phi)) = -\bar{\dot{E}}(x) - \frac{\partial \bar{Q}}{\partial \bar{x}}$$
$$\bar{Q} = -\bar{h}\bar{k}_p(\phi)\frac{\partial \bar{P}_c}{\partial \bar{x}}$$

$$\frac{\partial}{\partial \bar{t}}(\bar{h}\phi) = 0 \tag{12}$$

$$\bar{P}_c = \begin{cases} -\beta_e\left(1 - \dfrac{\phi_{rcp}}{\phi}\right)^2 & \text{(elastic particles)} \\ -\beta_v\left(1 - \dfrac{\phi_{rcp}}{\phi}\right)\dfrac{1}{\phi^2}\dfrac{\partial \phi}{\partial t} & \text{(viscous particles)} \end{cases}$$

where

$$P_c \equiv \bar{P}_c\left(\frac{\dot{E}_o l^2 \mu_w}{h_o R_o^2}\right)$$

$$k_p(\phi) \equiv \bar{k}_p(\phi) R_o^2$$

$$\beta_e \equiv \frac{3\nu\phi_{rcp} G h_o R_o^2}{28\dot{E}_o L^2 \mu_w}$$

$$\beta_v \equiv \frac{3\nu\phi_{rcp}^2 \mu_p R_o^2}{14 L^2 \mu_w}$$

At $\bar{x} = 0$, both the fluid flux, $\bar{Q}$, and the height of the film are zero. Note that the spatially varying evaporation rate, $\dot{E}(x)$, is rendered dimensionless with $\dot{E}_o$, where

$$\dot{E}_o = \frac{1}{L}\int_{x=0}^{L} \dot{E}(x)\, dx$$

While comparing the results with those obtained with experiments, the time variable is sometimes rendered dimensionless with $h_o(1 - \phi_o)/\dot{E}_o$ so that $\hat{t} \equiv \bar{t}/(1 - \phi_o) = 1$ corresponds to the end of drying.

Similarly, the dimensionless forms of the equations for the fluid domain are given by

$$\frac{\partial \bar{h}}{\partial \bar{t}} = -\bar{\dot{E}}(x) - \frac{\partial}{\partial \bar{x}}(\bar{h}\bar{u}_x)$$

$$\frac{\partial}{\partial \bar{t}}(\bar{h}\phi) = -\frac{\partial}{\partial \bar{x}}(\phi\bar{h}\bar{u}_x) \tag{13}$$

$$\bar{u}_x = \alpha \bar{h}^2 \frac{\partial^2 \bar{q}}{\partial \bar{x}^2}$$

$$\bar{q} = \frac{\partial \bar{h}}{\partial \bar{x}}$$

where

$$\alpha = \left(\frac{h_o}{L}\right)^4 \frac{\gamma_d}{3\mu_d \dot{E}_o}$$

At $\bar{x} = 1$, the height profile is symmetric and the fluid flux is zero, so the boundary conditions are simply $\bar{q} = 0$ and $\bar{u}_x = 0$. At the front that separates the fluid and the solid domains ($\bar{x} = \bar{x}_f$), both the film height and liquid flux are continuous, i.e.

$$\bar{h}|_{\bar{x}=\bar{x}_{f^-}} = \bar{h}|_{\bar{x}=\bar{x}_{f^+}}$$

$$\bar{Q}|_{\bar{x}=\bar{x}_{f^-}} = \bar{h}\bar{u}_x(1 - \phi)|_{\bar{x}=\bar{x}_{f^+}} \tag{14}$$

while the velocity of the front is determined from a particle balance across $\bar{x} = \bar{x}_f$

$$(\phi|_{\bar{x}=\bar{x}_{f^+}} - \phi|_{\bar{x}=\bar{x}_{f^-}})\frac{d\bar{x}_f}{d\bar{t}} = [\phi\bar{u}_x]_{\bar{x}=\bar{x}_{f^+}} \tag{15}$$

Equations 12 and 13 were discretized using the Galerkin finite element technique and solved using a commercially available numerical library (DIFFPACK[18]). The solution required some care, however, since the equations are nonlinear and strongly coupled the position of the front and therefore the size of the domains are functions of time. As an initial condition, we assumed a dimensionless height profile of $\bar{h} = 10.53\bar{x}$ for $\bar{x} < 0.1$ and $\bar{h} = 1.053$ for the remaining section which gives an average dimensionless height of unity. The initial concentration profile consisted of a small solid domain ($\bar{x} < 0.01$) at $\phi = \phi_{rcp}$ with the rest of the film at the initial dispersion concentration (ϕ_o). We found that in order to maintain numerical stability, especially at early times when the height and concentration profiles change considerably, a fully implicit scheme for the solid domain and a semiexplicit scheme for the fluid domain gave the best results. With values known at time $\bar{t}$, the unknowns at $\bar{t} + \delta\bar{t}$ were determined by first solving eq 15 to locate the position of the front at $\bar{t} + \delta\bar{t}$. The domains were then remeshed and the known values at time $\bar{t}$ were interpolated on to the new mesh. Next, the unknowns for the solid domain were determined at the new time from (12) with the boundary conditions of zero flux and zero height at $\bar{x} = 0$ and, $\phi = \phi_{rcp}$ and $\bar{h} = \bar{h}(\bar{t} + \delta\bar{t})$ at $\bar{x} = \bar{x}_f$. Interestingly, the above procedure requires the knowledge of the height at the front for the new time step, $\bar{t} + \delta t$, for determining the heights and concentrations at all other locations in the solid domain. We solved this problem by setting the height at the front to that obtained on solving the liquid domain equations (13), using the known values determined at $\bar{t} - \delta\bar{t}$ and $\bar{t}$. With all the unknowns determined on the solid side for $\bar{t} + \delta\bar{t}$, (13) was solved next to obtain height and concentration profiles for the fluid domain at the new time. Here, the continuity of flux and height at $\bar{x} = \bar{x}_f$ (eq 14) and $\bar{q} = \bar{u}_x = 0$ at $\bar{x} = 1$ served as the boundary conditions.

For film-forming dispersions that contain soft polymer spheres (such as WCFA in the present case), the particles at the edge of the film deform completely to form a transparent film. In such cases, two fronts propagate toward the center of the film; a "dry" front that separates the fully formed domain ($1.0 < \phi < \phi_{rcp}$) and "wet" front separating the saturated domain from the fluid domain. The governing eqs 12 and 13 are solved for the section of the film lying between the dry front and the center of the film and the computational domain was remeshed at every time step to accommodate the advancing dry front. During the computations, the dry front was advanced by an infinitesimal amount ($\sim 10^{-6}$) and eq 12 was solved subject to the condition of zero flux at the dry front. The magnitude of the advance was set by ensuring mass conservation of both particles and liquid.

Employing the procedure detailed above, the profiles of height, concentration, and capillary pressure were obtained as functions of time for given values of α and β_e (or β_v). From the constitutive relation (4) the corresponding transverse stresses follow as

$$\bar{\sigma}_{ij} = -\frac{4}{5}\bar{P}_c$$

Since the pressure in the solid domain scales as $\dot{E}_o L^2 \mu_w/(h_o R_o^2)$ and that in the fluid domain scales as $\mu_w L^2 \dot{E}_o/h_o^3$,

(18) Langtangen, H. P. *Computational Partial Differential Equations*; Springer-Verlag: Berlin, 1999.

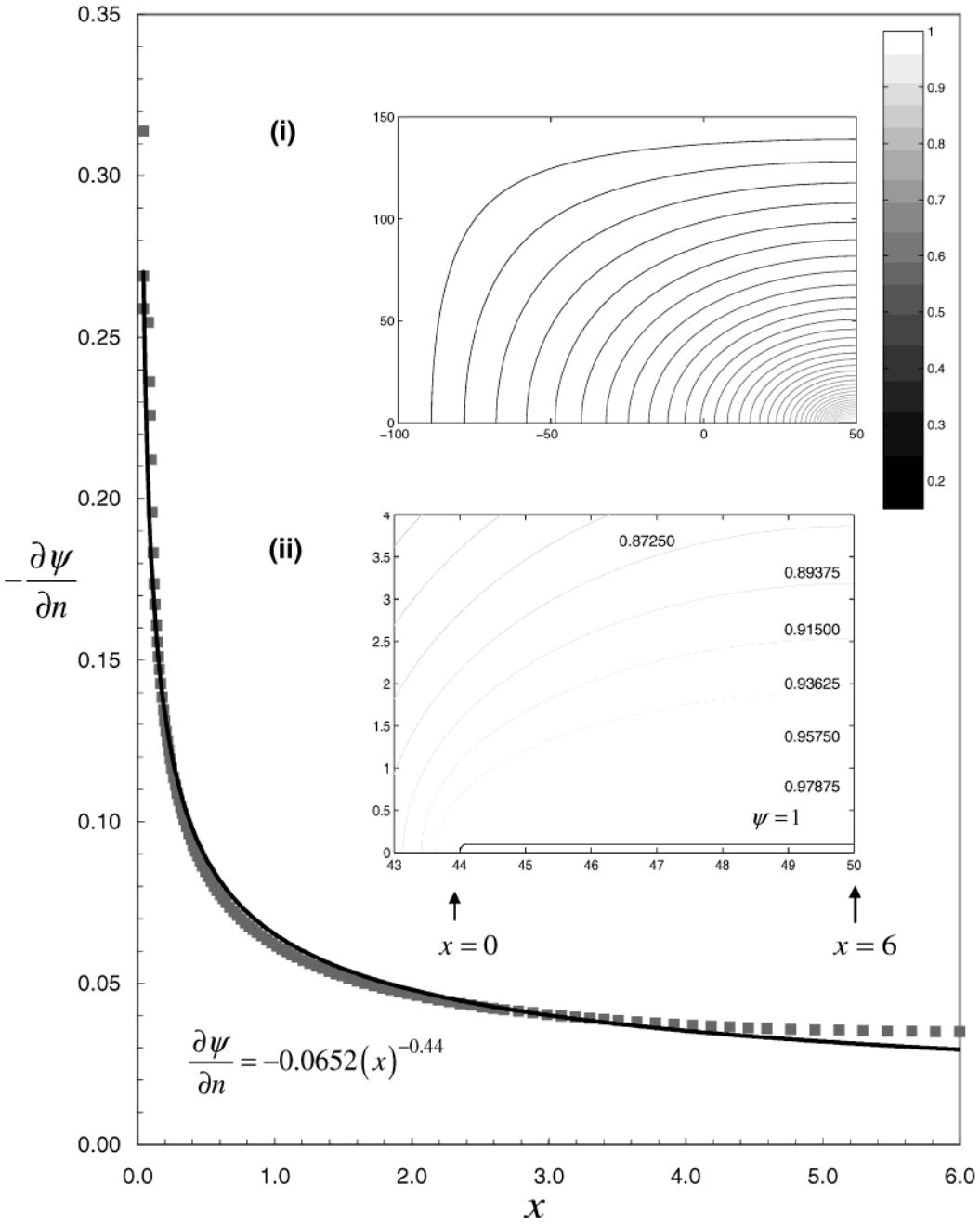

Figure 3. A plot of the concentration gradient at the film surface obtained from the numerical solution of the steady-state diffusion eq 16. The solid line is obtained from a power-law expression to fit the data. The insets (i) and (ii) contain the contours of the concentration profile. Note that the surface flux is given by, $\dot{E}(x) = -\mathcal{C}_{vap}\mathcal{D}(\partial\psi/\partial n)$, where $\mathcal{D}$ is the binary diffusion coefficient and $\mathcal{C}_{vap}$ is the saturated vapor concentration.

the ratio of the two pressures scales as h_o^2/R_o^2. Thus, for films with thicknesses much larger than the particle size, as in the present case, only contributions from the solid domain are significant.

One of the goals of this study is to compare the measured bulk stresses via the cantilever technique with those predicted by the model. Note, however, that while the model considers only one-dimensional propagation of the front, the induced stress in the experiment is two-dimensional and the fronts propagate from all four sides of the sample. To obtain an equivalent value of the bulk (transverse) stress, we assumed that the stresses and the corresponding front position predicted by the one-dimensional model apply to all sides. A schematic view of such an approximation is shown in Figure 2(a). The stresses and the film thickness were then averaged along the width to give the averaged transverse stress as a function of the spatial coordinate along the length of the film. The film was divided into small sections (along the length), and the contribution from each element to the deflection angle, calculated from eq 1, was added to obtain the total deflection of the substrate. Finally, eq 1 was used once again to obtain the bulk stress from the previously calculated value of total deflection and the known values of film length and average height. For the film-forming case, the stresses in both the fully formed and saturated regions were accounted for while calculating the total bulk stress in the film.

4. Results and Discussions

4.1. Evaporation Experiments. It is well-known that when a sessile drop of water with a pinned contact line

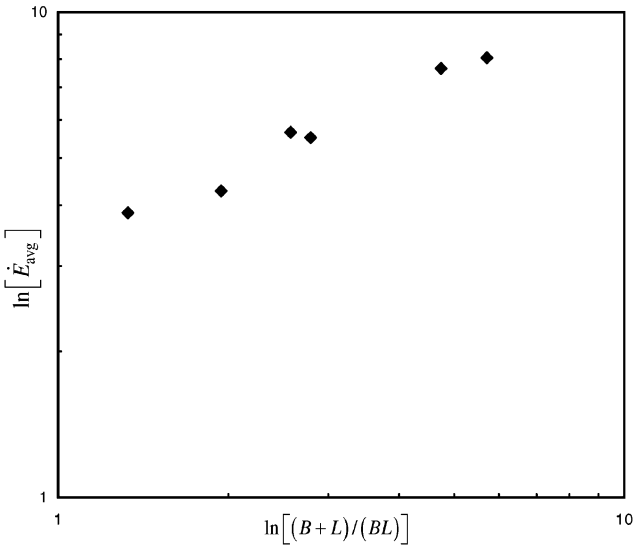

Figure 4. A log−log plot of the measured evaporation rate for thin films of PPG342 dispersions as a function of the ratio of the perimeter to the area of the film. The initial concentration of the dispersion was 0.46 while the average height of the films varied from 100 to 270 μm. The ambient temperature and relative humidity were, respectively, 23 °C and 15%.

evaporates in the absence of forced/natural convection such that the mass transfer is dominated by diffusion, the evaporation flux varies spatially with the highest flux observed at the edges of the drop.[4,19] For millimeter sized drops, diffusion time scales are small compared to the total evaporation time so that the evaporation process is pseudosteady. Although the dimensions of our films are somewhat larger (tens of millimeters), drying occurs inside an enclosed chamber thereby eliminating forced convection. To investigate this further, we recorded the weight of films of various dimensions, dried under identical conditions, as a function of time.

Figure 4, presents the measured average evaporation rate as a function of the ratio of the film perimeter, $4(B + L)$, to the total film area, $4BL$, where $2B$ and $2L$ are, respectively, the length and width of the film. Note that this ratio characterizes the specific edge length and also differentiates films having the same area but different aspect ratios. The average film thickness varied between 100 and 270 μm but did not affect the rate. The evaporation rate increases monotonically with increasing perimeter (per unit area), doubling from 1.3 to 5.7 cm^{-1}. This plot clearly demonstrates the power-law dependence of evaporation rate on the film dimensions.

Next, we solved the diffusion equation in order to estimate the evaporation rate under conditions of negligible natural/forced convection. The governing equation

$$\partial^2\psi/\partial x_j^2 = 0 \qquad (16)$$

where ψ is the ratio of the vapor concentration, $\mathscr{C}$, to the saturated vapor concentration, $\mathscr{C}_{vap}$, was solved subject to the boundary condition that the vapor concentration equals the saturated vapor concentration at the surface of the film and approaches the ambient concentration, $\mathscr{C}_\infty$, at infinity. In addition, the flux is zero normal to the surface of the substrate around the drop. Deegan et al.[4] and Hu and Larson[19] have recently calculated for a spherical cap drop evaporation rates from the numerical solutions of the governing equation in close agreement with measured values. As expected, the large concentration gradient at the edge of the drop results in high evaporation fluxes that decrease monotonically toward the center. On the basis of these results, Deegan et al.[4] fit the spatially varying flux to a simple power law expression and found the exponent to vary with the contact angle, approaching 0.5 at zero contact angle.

We solved numerically the two-dimensional form of eq 16 for elliptical and square (with round ends) film profiles with the PDEtoolbox software of MATLAB, which utilizes the standard Galerkin finite element technique for solving partial differential equations. Figure 3 presents the normalized concentration gradient, normal to the surface of the film, for a square film along with a contour plot of the normalized concentration in the inset. The dimensions of the film, namely, the height and the width, correspond to the typical dimensions achieved in the experiments. Note that the flux follows a simple power law that varies little with the shape of the film from 0.44 for the square film to 0.41 for the elliptical film. The contour plot for the concentration shows clearly the larger gradients at the edge of the film. The numerical results were insensitive to the size of the domains exceeding approximately 20 times the width of the film.

The measured average evaporation rates were compared with those calculated from eq 16 as

$$\dot{E}_o = \frac{2\mathscr{D}\mathscr{C}_{vap}}{\rho_w L}\int_{x=0}^{x=L}\left|\frac{\partial\psi}{\partial n}\right|_{surface} dx$$

with ρ_w the density of (liquid) water. The measured rates were approximately twice the value obtained by solving eq 16 for those calculated for films of equivalent widths. Thus the actual rate appears to be enhanced by natural convection.

The importance of natural convection can be estimated from the magnitude of the Grashoff number which signifies the balance between the driving force of buoyancy and the resisting inertial forces

$$Gr \equiv \frac{g(2L)^3\rho_\infty(\rho_{vap} - \rho_\infty)}{{\mu_\infty}^2}$$

Here, g is the gravitational acceleration, μ_∞ and ρ_∞ are, respectively, the ambient air viscosity and density, while ρ_{vap} is the density of air saturated with vapor at the ambient temperature. For a wet film of width 12 mm, air viscosity of 1.8×10^{-5} Pa·s, air density (15% relative humidity and 24 °C) of 1.286×10^{-6} g/mm^3, and a saturated air density (24 °C) of 1.274×10^{-6} g/mm^3, the Grashoff number is approximately 820. Since the ratio of the flux with the natural convection to the diffusion flux generally varies as $Gr^{1/4}$, this suggests an enhancement factor of $\mathscr{O}(5)$, consistent with the observation.

Since the determination of the spatially varying evaporative flux in the presence of natural convection is a complex problem, we retained the power law form of the flux, $\dot{E}(x) = Ax^{-\lambda}$, determined from the diffusion equation with the multiplicative constant A, calculated by setting the total evaporation rate to the measured value. In all our computations, the exponent, λ, was assigned a value of 0.44.

4.2. Stress Measurements. As noted earlier by Petersen et al.,[17] the present experimental technique results in a delay of approximately 1−2 min between the application of the coating and the start of data acquisition. As a result, the measured deflection deviates from the

(19) Hu, H.; Larson, R. G. Evaporation of a sessile droplet on a substrate. *J. Phys. Chem. B* **2002**, *106*, 1334−1344.

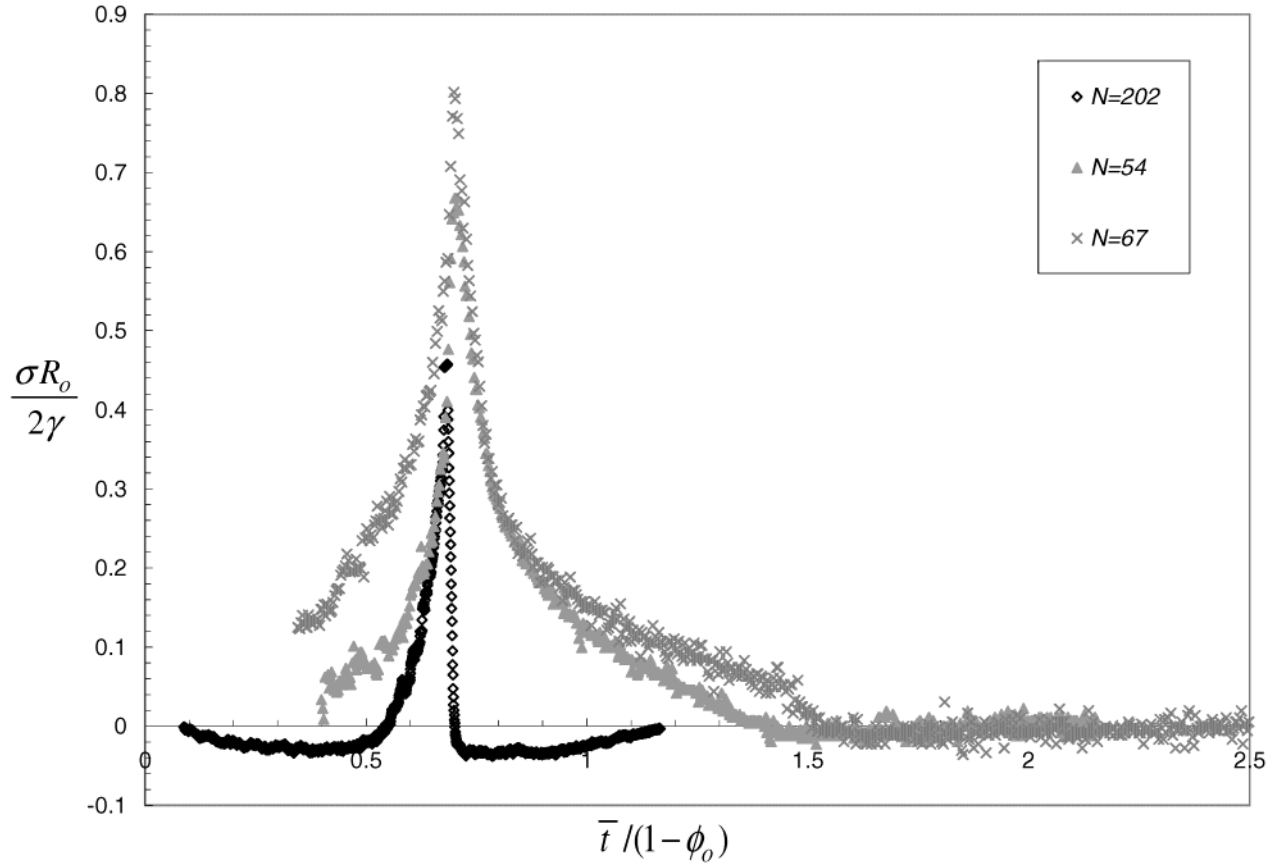

Figure 5. A plot of the dimensionless stress measured as a function of dimensionless time for various initial film thicknesses for the PPG342 dispersion of concentration 0.38.

true value by an amount that corresponds to the net deflection experienced by the substrate before the start of the data acquisition. To compensate, the measured values were extrapolated to zero time to determine the shift. Except for very thin films, the magnitude of this shift factor was negligible. It should be noted, however, that in the case of the non-film-forming latices, the shift value can be determined directly from experiments since the cracks toward the end of the drying process cause the deflection to fall to a negligible value.

4.2.1. Non-Film-Forming Latices. Figures 5 and 6 present the bulk stress (eq 1), rendered dimensionless with the characteristic capillary pressure ($2\gamma/R_o$), for PPG342 of initial volume fractions of 0.50 and 0.38, respectively, as a function of dimensionless time, $t\dot{E}_o/(h_o(1-\phi_o))$, over a range of dimensionless film thicknesses, $N \equiv h_o\phi_o/(2R_o\phi_{rcp})$. A similar plot of the GMA610 dispersion for a particle volume fraction of 0.49 is presented in Figure 7. Two distinct phases of stress increase are observed for both dispersions, irrespective of the film thickness. The stress increases slowly with evaporation with intermittent drops during the first phase. Although the origin is not clear, these fluctuations could be caused by either large scale movement of particles in the packed domain, such as layers sliding past each other, or slip at the particle−substrate interface. The onset of the second phase is marked by a sharp increase in stress resulting in a profile that is smooth. Thus, the mechanism causing the stress fluctuations in the former case is apparently absent during this phase. After a peak value is attained, for thick films, the stress falls rapidly to a negligible value. The sharp decline coincided with the appearance of cracks. For thinner films, however, the decay in stress is more gradual even in the presence of cracks and continues well beyond $\bar{t}/(1-\phi_o) = 1$. Interestingly, for both dispersions, irrespective of the film thickness or initial particle concentration, the peak stresses occur when the average particle concentration is about 0.68 and not at $\bar{t}/(1-\phi_o) \sim 1$; the latter corresponds to the end of the drying process. Weight loss experiments (Figure 8) performed on the GMA610 dispersion detect a constant evaporation rate until the very end of the drying process with no effect of the cracks.

A visual inspection of the drying film revealed two distinct regions, a central wet region containing a fluid dispersion surrounded by a close-packed domain of a much higher volume fraction. As drying proceeds, the central wet region shrinks uniformly from all sides and the packed domain remains saturated. The first phase of stress increase occurs during the growth of the solid domain, while the onset of the second phase coincides with the disappearance of the fluid domain and the appearance of a dimple at the center of the film. The stress maximum and the subsequent drop in the stresses coincide with the appearance of cracks throughout the film. Chiu and Cima[13] have reported similar observations for the drying of thin films of aqueous alumina dispersions.

A plot of the peak stress scaled on the nominal capillary pressure as a function of dimensionless film thickness for PPG342 ($\phi_o = 0.50$ & 0.38) and GMA610 ($\phi_o = 0.49$) dispersions in Figure 9 collapses the data for both particle sizes, especially at small film thicknesses ($N < 200$). These results indicate that the bulk stress originates from the capillary pressure induced by the liquid menisci between particles. Interestingly, the peak stress decreases with increasing film thickness, indicating that the thinner films are able to sustain larger tensile stresses before cracking. The situation discussed here is analogous to the cracking

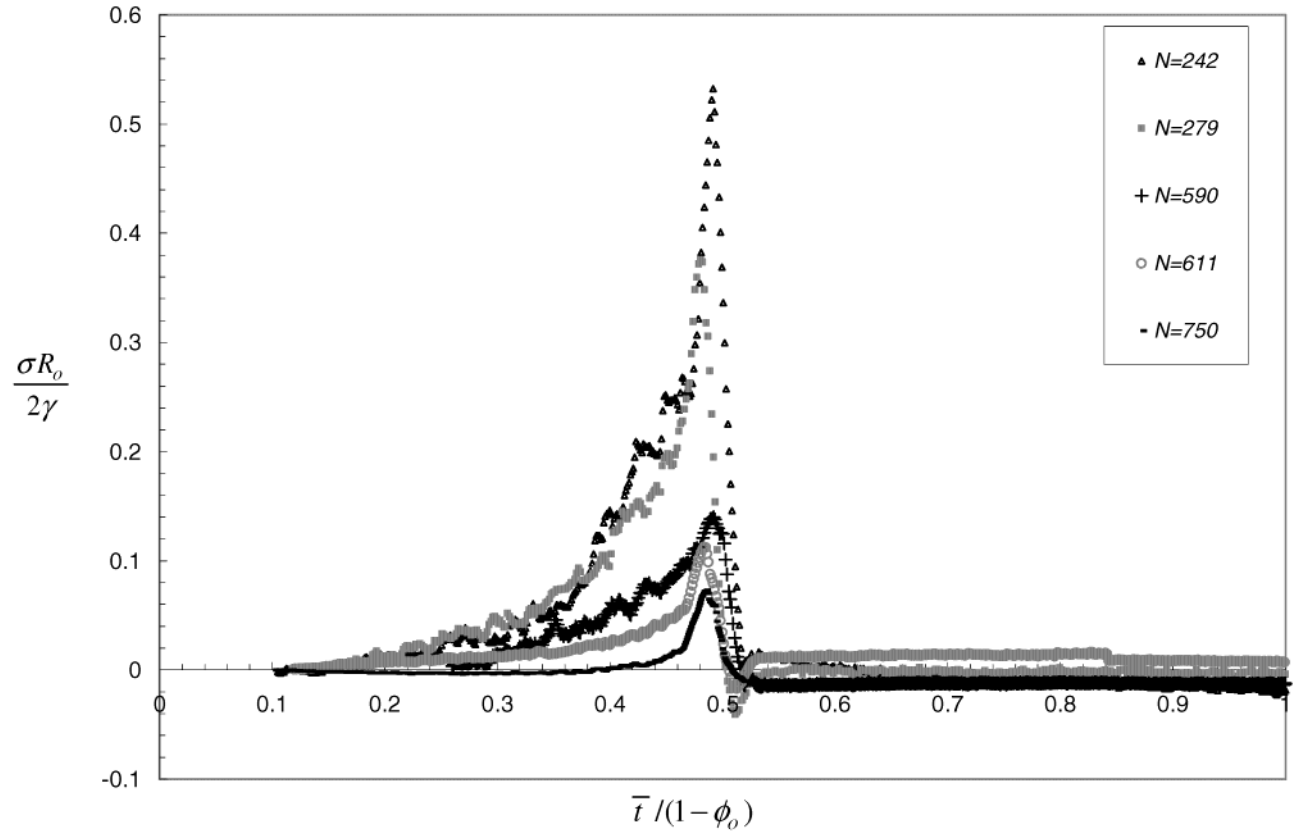

Figure 6. A plot of the dimensionless stress measured as a function of dimensionless time for various initial film thicknesses for the PPG342 dispersion of concentration 0.50.

of thin elastic films under residual tensile stress bonded to an elastic substrate. Applying the well-known Griffith's criterion for brittle fracture, which balances the elastic energy recovered by crack propagation against the energy required to create new surface, Evans et al.[20] predict the stress at cracking to vary inversely with the square root of the film thickness (see Figure 9). The peak stresses presented in Figure 9 follow a similar trend at small thicknesses but exhibit significant deviations at larger thicknesses. This is not altogether surprising since the present case differs from that considered by Evans et al.[20] in that the recovery of the elastic energy is effected by the presence of fluid in the pores between particles. However, their analysis guided our understanding of cracking in latex films and motivated a detailed treatment to be presented in a separate publication.

4.2.2. Film-Forming Latices. Figure 10 presents the stress development for the WCFA dispersion for various initial film thicknesses. The stress increase, in contrast to the non-film-forming dispersions, is more gradual and attains a maximum at the end of the drying process ($\bar{t}/(1 - \phi_o) \sim 1$). Visual observation of the drying film reveals three distinct domains, viz., a central white region containing the dilute dispersion, an outer transparent domain where the film is either fully formed or the particle deformation has caused the pore size to decrease below the wavelength of the visible spectra, and a small translucent region separating the aforementioned two regions. The fluid domain shrinks with drying and disappears at the end of the drying process, leaving behind a fully transparent film. As in the case of the non-film-forming dispersion, a dimple is formed at the center of the film which coincides with the disappearance of the wet region. Weight loss experiments show (Figure 11) that the average rate of drying is higher initially and decreases slightly as the wet region shrinks and the outer domains undergo particle deformation to form a transparent film. Recall that similar weight loss experiments for the non-film-forming dispersions resulted in a more or less a constant decrease of sample weight with time. These results agree well with observations of Martinez and Lewis for dispersions containing particles of similar glass transition temperature (~19 °C). For $\bar{t}/(1 - \phi_o) > 1$, when all the water has evaporated and, consequently, the capillary stresses are absent, the tensile stress exerted by the substrate deforms the film and lowers the bulk (residual) stress in the film. In almost all cases, the stress initially decreased for $\bar{t}/(1 - \phi_o) > 1$ and attained a constant but finite value at long times. This seems to suggest that the film binds strongly to the substrate and the interfacial slip between the film and the substrate, if any, is negligible.

The peak stresses, as for the non-film-forming dispersions, decrease with increasing film thickness (Figure 12). However, for comparable film thicknesses, the maximum stresses attained for the film-forming dispersion are lower than those observed for the non-film-forming dispersions (PPG342 and GMA610). For film-forming dispersions, the particles deform viscously under capillary forces, thereby reducing the bulk stress in the film. In the case of the elastic particles (PPG342 and GMA610), however, the large shear modulus of the particles permits only small deformations and causes the stress to increase to large values. The induced stresses are then relieved by either cracking or slip between particle layers or the film and the substrate. Interestingly, all three dispersions, irrespective of the particle size or glass transition temper-

(20) Evans, A. G.; Drory, M. D.; Hu, M. S. The cracking and decohesion of thin films. *J. Mater. Res.* **1988**, *3*, 1043−1049.

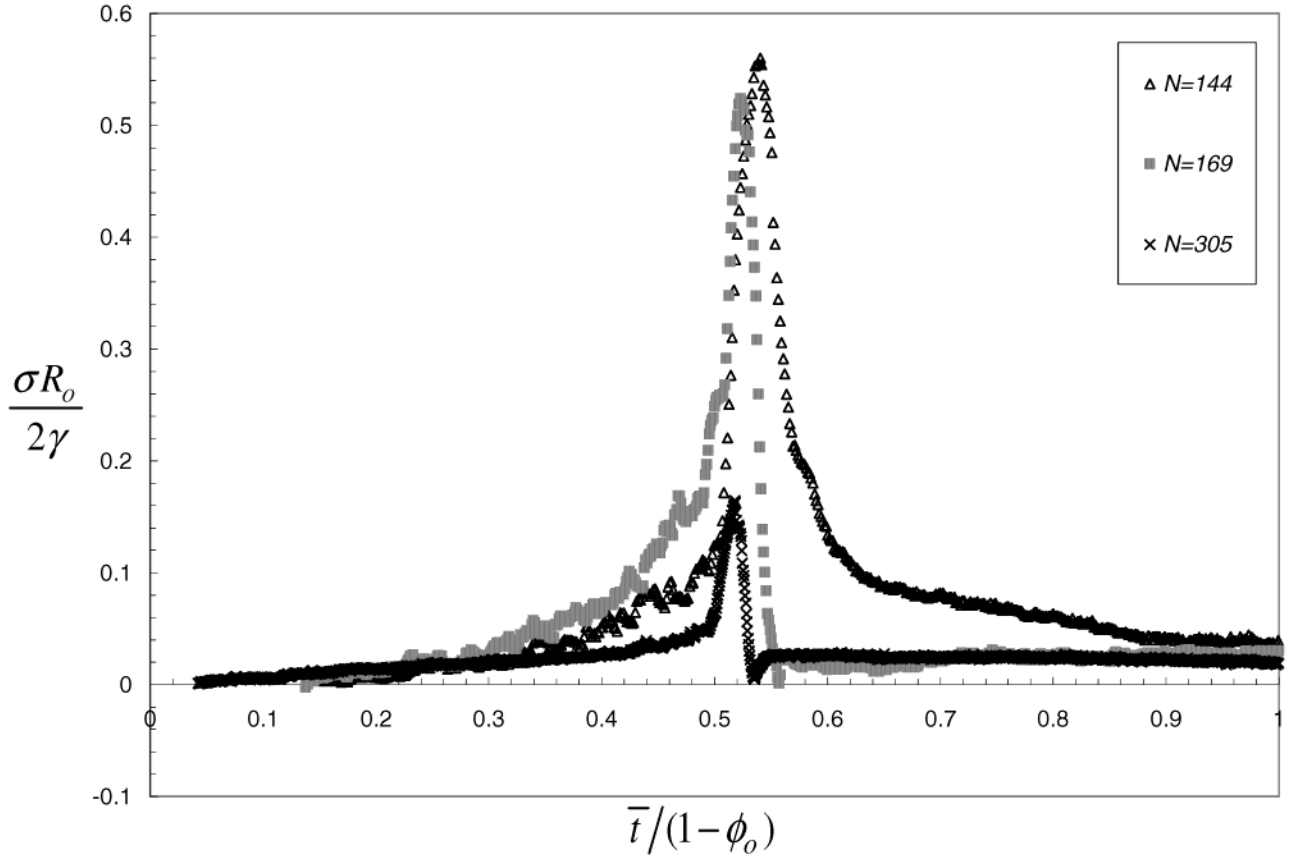

Figure 7. A plot of the dimensionless stress measured as a function of the dimensionless time for various initial film thicknesses for the GMA610 dispersion of concentration 0.49.

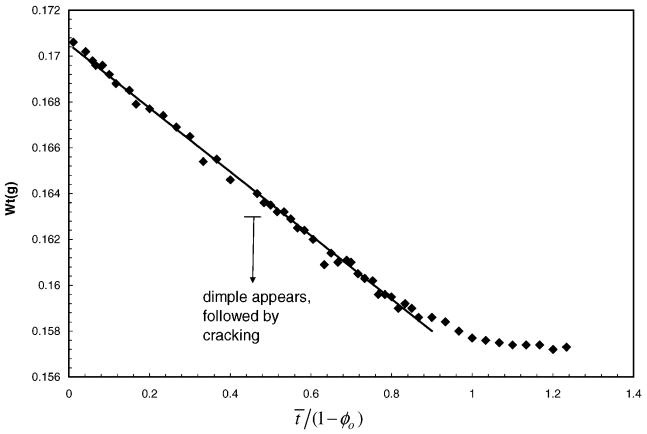

Figure 8. Weight loss experiment as function of dimensionless time for the GMA610 dispersion of concentration 0.49 and an initial film thickness of 155 μm.

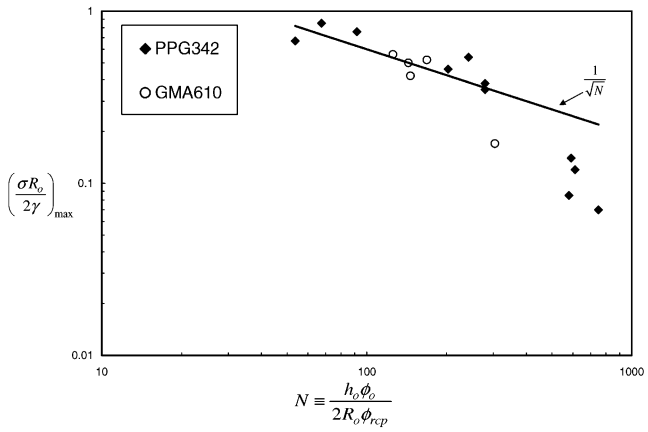

Figure 9. A plot of the maximum stress measured as a function of the film thickness for PPG342 and GMA610 dispersions.

ature, show similar dependence of peak stress (dimensionless) on the dimensionless film thickness.

4.3. Computations and Comparison with Experiments. We computed the concentration, height, and stress profile for the various experiments listed in Tables 2 and 3 that correspond to, respectively, the non-film-forming (PPG342 and GMA610) and film-forming (WCFA) dispersions. A random closed packing concentration of 0.67 was assumed for all computations. Before proceeding further it is worth noting that except for the values of the dispersion viscosity (μ_d), particle viscosity (μ_p), and solvent viscosity(μ_w), all the parameters listed in Tables 2 and 3 were obtained directly either from our experiments or from standard handbooks (e.g., *G*). Though the values of μ_d and μ_p were estimated to fit the stress data, the assumed values are close to those expected. A solvent viscosity of approximately 2 mPa·s was assumed taking into account the effect of dissolved salts in the dispersion.

The solution of the governing equations for the particle deformation along with the spatially varying evaporation rate was straightforward for the non-film-forming case with the iterations converging at every time step. For the film-forming case, however, the infinitely high flux at the edge of the film ($\bar{x} = 0$) caused the program to diverge. We were able to circumvent this problem by retaining the power-law flux for $0.005 < \bar{x} < 1.0$ and assigning a constantflux of $\dot{E}(x) = A(0.005)^{-\lambda}$ for $\bar{x} < 0.005$. Note that the multiplicative constant, *A*, was determined, as before, by setting the total evaporation rate to the measured value.

4.3.1. Non-Film-Forming Latices. Figure 13 presents, for experiment no. 2 (Table 2), the spatial variations of

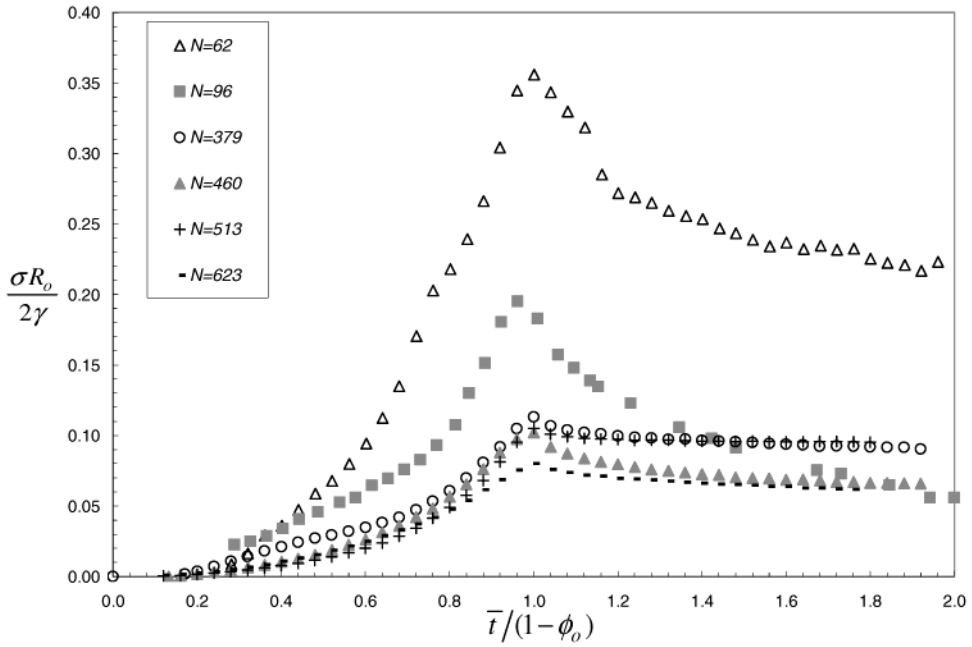

Figure 10. A plot of the dimensionless stress measured as a function of the dimensionless time for various initial film thicknesses for the WCFA dispersion for volume fractions in the range of 0.32−0.35.

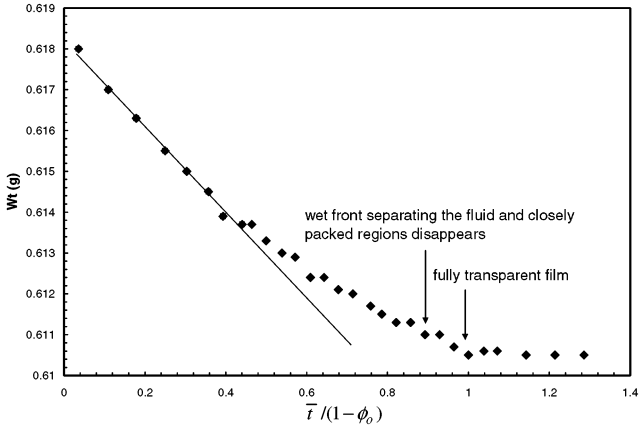

Figure 11. Weight loss experiment as function of dimensionless time for the WCFA dispersion of concentration 0.32 and an initial film thickness of 45 μm.

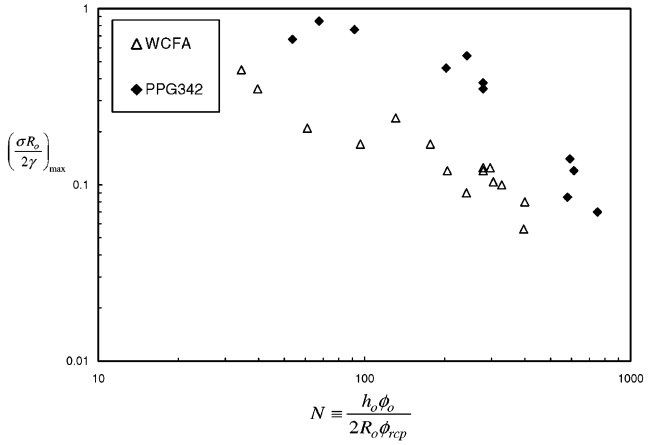

Figure 12. A plot of the maximum stress measured as a function of the film thickness for the film-forming (WCFA) and non-film-forming (PPG342) dispersions for volume fractions in the range of 0.32−0.35.

the nondimensional height and particle concentration at various times after the start of the drying process. The front between the solid and fluid domains is marked by the sudden drop in particle concentration from the random closed packed value on the solid side to the lower value on the fluid side. As expected, the overall height of the film decreases with time while the total particle concentration increases. The particle concentration in the solid domain increases monotonically from the closed packed value at the front to the maximum value at the edge. The magnitude of the variation, however, is minimal since a small strain or, equivalently, a small concentration increase is sufficient to maintain the requisite capillary pressure for drawing the solvent into the solid domain. As a result, the particle fraction at the edge of the film increases by a small amount from 0.67 to 0.682 after 0.51 dimensionless time units. In the fluid domain, the height profile is set by a balance of the pressure induced by gradients in film curvature with the opposing viscous stresses. The fluid domain satisfies the required negative liquid flux at the front by assuming a negative film curvature close to the front and a positive curvature far away. Thus the curvature is small for initial times and increases with increasing size of the solid domain. The concentration profile in the fluid domain, on the other hand, is determined by a balance of fluid convection and evaporation that results in low particle concentrations in regions of large film thickness. The front moves slowly at short times propagating about 0.25 spatial units in the initial 0.20 time units, before speeding up later to encompass twice the distance in the same amount of time (from $\bar{t}/(1 - \phi_o) = 0.20$ to 0.40). This increase in front velocity can be understood from the boundary condition (15) since, as drying proceeds, the increase in the length of the solid domain requires the solvent flux at the front to increase. This is further augmented by the deposition of more particles due to the steadily increasing particle concentration in the fluid domain. Finally, as the front reaches $\bar{x} = 1.0$, a dimple forms at the center of the film. The depth of the dimple is affected by the concentration difference between the fluid and the solid domains at the front with deeper dimples formed at large concentration differences.

Table 2. Details of the Experimental Parameters for PPG342 and GMA610 Films Used in Computations[a]

no.	dispersion	ϕ_o	h_o (μm)	$\dot{E}_o$ (μm/min)	μ_d (Pa·s)	G (MPa)	L (mm)	B (mm)	α	β_e
1	PPG342	0.379	53	3.0	0.15	4200	6.35	10.7	0.015	5.9×10^5
2	PPG342	0.505	104	3.1	2.0	4200	6.5	10.1	0.015	1.1×10^6
3	GMA610	0.492	100	4.4	2.0	1700	6.0	11.7	0.013	1.1×10^6
4	GMA610	0.492	242	3.6	2.0	1700	6.5	10.0	0.384	2.8×10^6

[a] Note that the shear modulus, G, of the particles in the PPG342 and GMA610 dispersions are that of poly(styrene) and poly(methyl methacrylate), respectively. The viscosity of the solvent was assigned a value of 0.0019 Pa·s while the dispersion surface tension (γ_d) was assigned a value of 72 mN/m.

Table 3. Details of the Experimental Parameters for WCFA Films Used in Computations[a]

no.	ϕ_o	h_o (μm)	$\dot{E}_o$ (μm/min)	μ_d (Pa·s)	μ_p (Pa·s)	L (mm)	B (mm)	α	β_v
1	0.354	145	5.6	1.5	7.5×10^8	5.55	10.05	0.08	13.7
2	0.354	230	4.5	1.5	7.5×10^8	6.4	9.9	0.35	10.3
3	0.321	45	1.8	1.5	7.5×10^8	6.6	9.9	0.001	9.7

[a] The viscosity of the solvent was assigned a value of 0.0025 Pa·s while the dispersion surface tension (γ_d) was assigned a value of 72 mN/m.

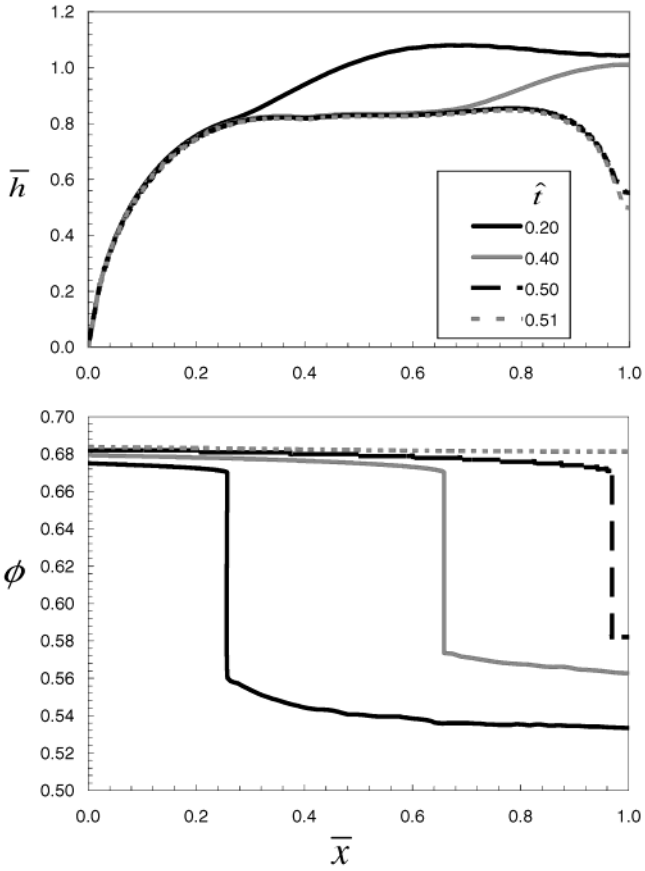

Figure 13. A plot of the height and concentration profiles obtained from computations for experiment 2 (PPG342) in Table 2 at various dimensionless times, $\hat{t} \equiv t\dot{E}_o/(h_o(1 - \phi_o))$.

The predicted height and concentration profiles for experiment no. 4 (Table 2) with the GMA610 dispersions are presented in Figure 14. Recall that the initial height profile consists of a linearly increasing height of slope, 10.53 for $\bar{x} < 0.1$ and a constant height of 1.053 for the rest of the film. However, the height profile at $\hat{t} = 0.198$ is far from that prescribed initially and differs markedly from that observed at a similar time for experiment no. 2 (Table 2). The dominant force of surface tension, signified by the large value of α, causes the height to vary slowly over the length of the film, resulting in a profile that is close to a

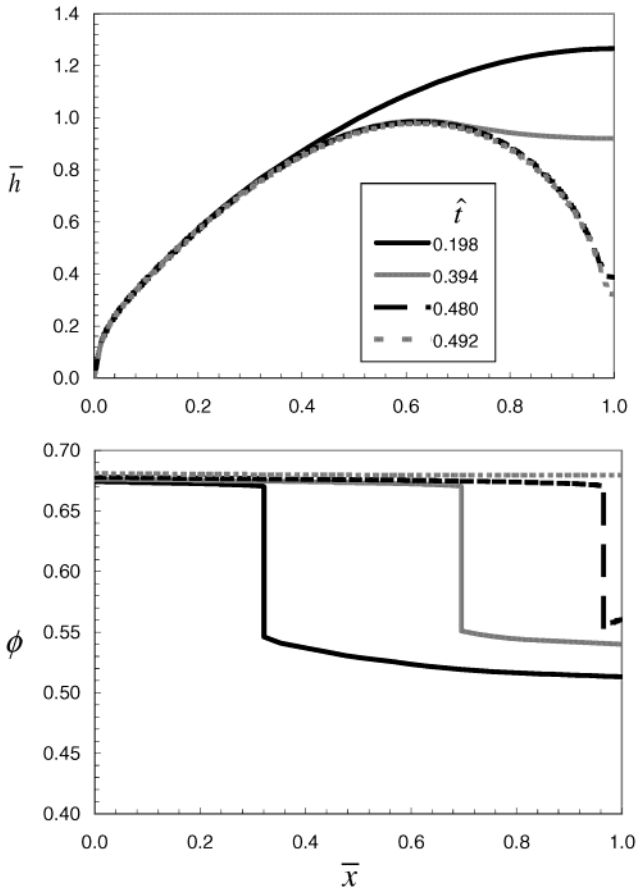

Figure 14. A plot of the height and concentration profiles obtained from computations for experiment 4 (GMA610) in Table 2 at various dimensionless times, $\hat{t} \equiv t\dot{E}_o/(h_o(1 - \phi_o))$.

spherical cap. It appears that the large value of α which results from the relatively large initial film height is also responsible for the formation of the deep dimple at $\bar{x} = 1$. As before, concentration variations in the solid domain are minimal, suggesting that modest deformation is sufficient to draw the solvent from the fluid domain into the solid.

We next compare, in Figures 15 and 16, the rising part of the measured bulk stress with the values predicted for the four experiments listed in Table 2. The stress increases slowly during the initial stages of the drying process since only a small section of the film is encompassed by the saturated solid domain and a minimal rate of strain is sufficient to draw the liquid from the fluid domain into the saturated domain. As the front propagates toward the center of the film, the stress rises at a rate that is close to that observed experimentally. The disappearance of the fluid domain is marked by a sharp increase in the stress since, in the absence of the fluid domain, the capillary stresses deform the particles at a rate set by evaporation. The model captures well the entire stress

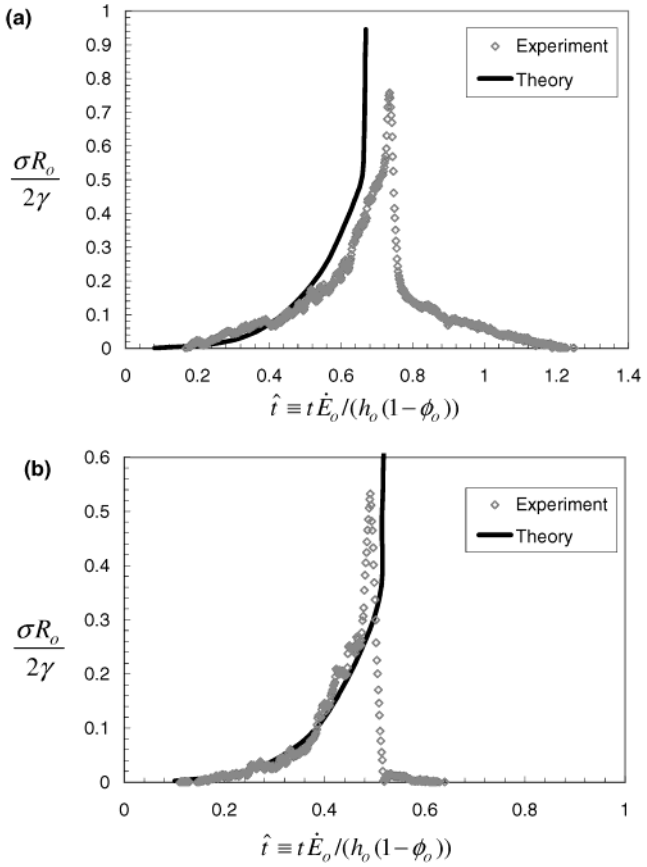

Figure 15. A comparison of the predicted bulk stress with the observed values for experiments (a) 1 and (b) 2 with the PPG342 dispersion. The parameters for each of the experiment are listed in Table 2. As mentioned earlier, the sharp increase in stress, which marks the onset of the second phase of stress increase, coincides with the disappearance of the fluid domain.

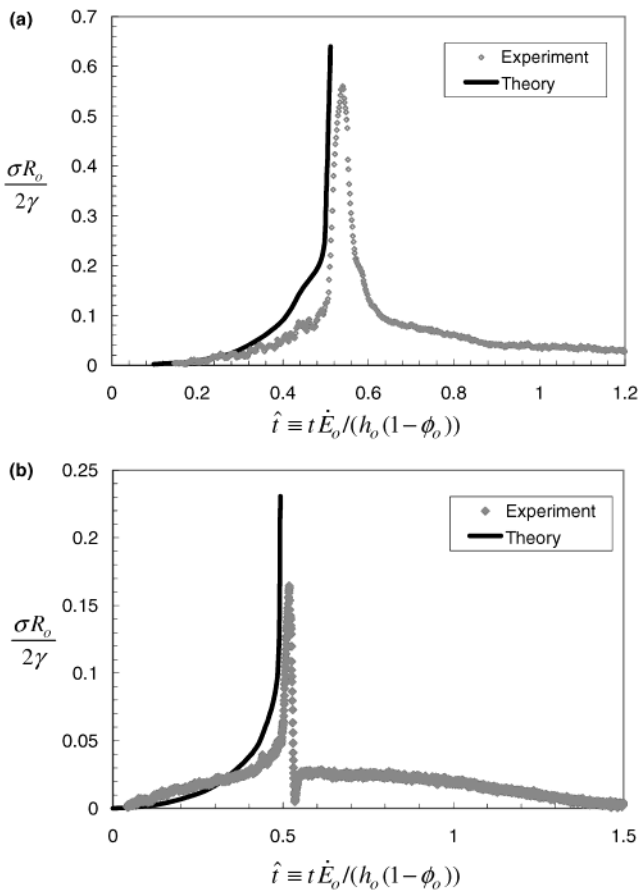

Figure 16. A comparison of the predicted bulk stress with the observed values for experiments (a) 3 and (b) 4 with the GMA610 dispersion. The parameters for each of the experiment are listed in Table 2. The sharp increase in stress, which marks the onset of the second phase of stress increase, coincides with the disappearance of the fluid domain.

profile for both the PPG342 films even though the initial particle concentration and the initial average film thickness are larger for experiment no. 2. There are, however, small deviations close to the peak stresses. A similar trend is observed with the GMA610 dispersion that contains larger particles. The overall agreement between the model predictions and the experimental results for experiments 2 (PPG342) in Figure 15b and 3 (GMA610) in Figure 16a, which have similar values of α and β_e, implies that the model captures correctly the influence of particle size on the deformation and drying processes.

In addition to the stress measurements, the position of the front was also monitored during the drying process. Figure 17 compares the position of the front, measured at two locations in the film, with that predicted by the model for experiment 2 (Table 2). A sketch of the drying film in the inset depicts the two-dimensional nature of the front propagation. As expected, the propagation was slower along the central section (i.e., along B) of the film. The measured position increases steadily at both locations (A and B) with the front velocity increasing only toward the end. Although the predicted saturated domain size is somewhat smaller than that observed experimentally along B, the predicted values follow the observed trend. The lower values of the predicted front position are responsible for the small deviations observed in the predicted bulk stresses compared with the measured values (Figure 15b). Figure 18 compares the front position for experiment 4 (Table 2) performed with the GMA610 dispersion with the model prediction. However, in this case, the observed front position, at the central section of

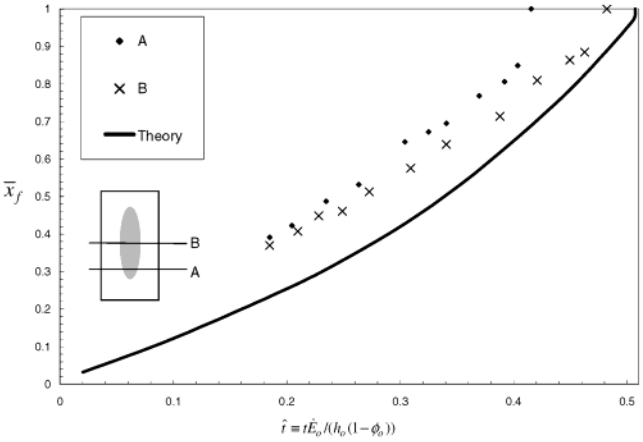

Figure 17. A comparison of the wet front position, $\bar{x}_f$, predicted for experiment 2 (Table 2) with that measured along sections, A and B, in the film.

film, lags the prediction, in accord with the slightly lower stresses compared to the predicted values in Figure 16b.

4.3.2. Film-Forming Latices. We next compare the results of the model predictions for the film-forming dispersions, WCFA, with the experimental observations. Figure 19 presents the height and concentration profile at various times for experiment 2, details of which are listed in Table 3. As observed previously in Figure 14a, the relatively large value of α results in a film that, at short times, resembles a spherical cap profile. However,

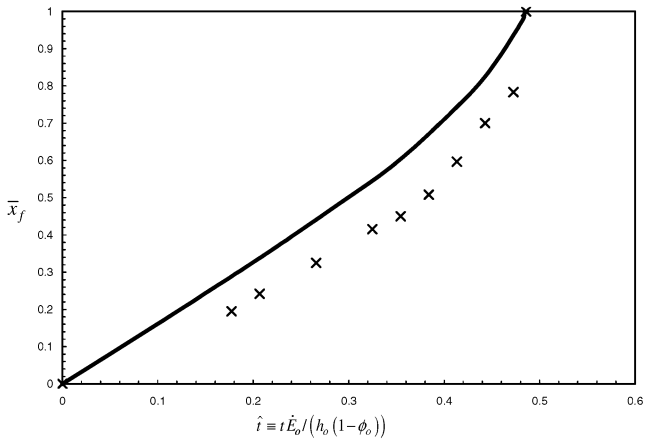

Figure 18. A comparison of the wet front position, $\bar{x}_f$, predicted for experiment 4 (Table 2) with that measured along the central section of the film.

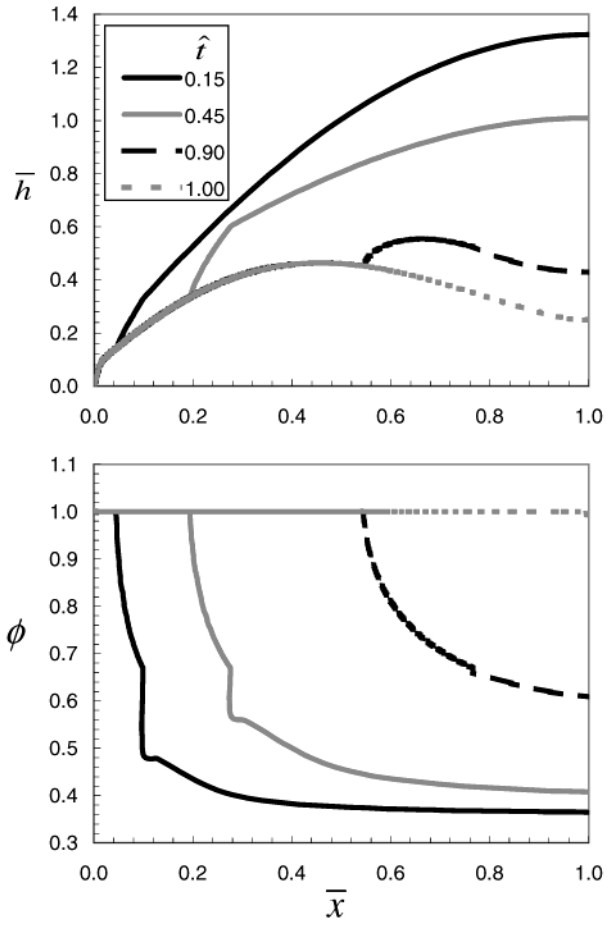

Figure 19. A plot of the height and concentration profiles obtained from computations for experiment 2 (WCFA) in Table 3 at various dimensionless times, $\hat{t} \equiv t\dot{E}_o/(h_o(1-\phi_o))$.

the presence of the dry domain causes the height profile to change slope at the drying front. Thus there are two distinct variations in the height profile that occur at the wet and the dry front. A depression is formed at the center of the film, but the height variations are smooth and the depression is shallower and broader than for the non-film-forming dispersion. These observations agree qualitatively with the height profiles measured by Martinez and Lewis for films cast from dispersions containing low and high T_g particles. In contrast to the non-film-forming dispersions, three different domains are observed in the

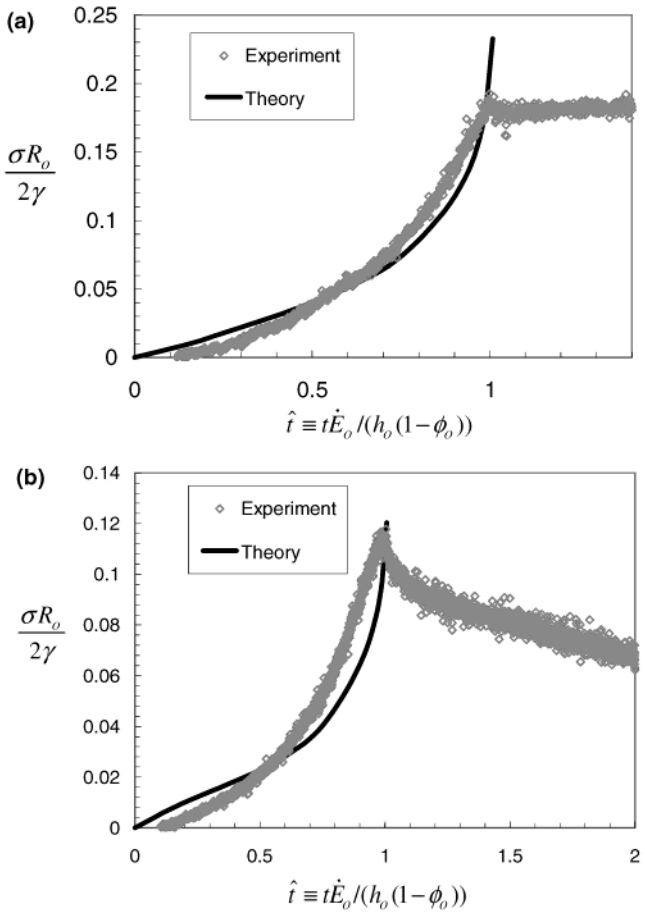

Figure 20. A comparison of the predicted bulk stress with the observed values for experiments (a) 1 and (b) 2 performed with the WCFA dispersion. The parameters for the experiments are listed in Table 3.

drying film. The outermost region contains the fully formed film ($\phi = 1.0$), which is devoid of water as the particles have deformed completely to fill the voids. The central part of the film contains the fluid dispersion and is surrounded by the saturated domain ($1.0 < \phi < \phi_{rcp}$). Unlike the non-film-forming dispersions, the particles in the present case undergo viscous deformation in the solid domain under the pressure required to draw the solvent from the fluid domain. As a result the induced capillary pressure is proportional to the rate of strain rather than the strain itself. Thus for low T_g particles, as in the present case, the particle concentrations in the saturated domain are much higher than those achieved for the nonfilm dispersions. This can be seen in the concentration profiles at $\hat{t} = 0.15$ and 0.45, where the particle fraction increases from that for a random closely packed array at the wet front to unity over a very short distance. The wet and dry fronts propagate at approximately the same rate for $\hat{t} < 0.45$. However, at longer times the wet front accelerates, thereby increasing the width of the saturated domain. The latter increase is caused by the deposition of a larger fraction of particles at the wet front due to the steadily increasing particle concentration in the fluid domain.

The rising part of the measured stresses for experiments 1 and 2 (table 3) are compared with the predicted values in Figure 20. The model predicts higher stresses for thinner films, which is in agreement with the trend observed experimentally. Although the peak stress for experiment 2 is slightly smaller than that predicted, there is excellent overall agreement between theory and experiments for both the films. The model predicts both the initial slow

increase and the sharp rise of the stress toward the end of the evaporation. These results show that the model captures all the salient features of stress development observed for a drying film.

Finally, Figure 18 compares the measured wet and dry front position with those predicted by the model. Here, in contrast to the non-film-forming case, there is some disagreement as the model under predicts the location of both fronts. The observed rate of propagation is greater at initial times with almost a linear increase in front position with time. Interestingly, the measured width of the saturated domain, which is the region between the dry and wet fronts, is also larger. Despite these deviations, the model captures the overall trend of front propagation.

5. Conclusion

Films cast from aqueous dispersions containing spherical particles of different sizes and glass transition temperatures were dried to understand the influence of various factors on the stresses induced during drying. Dispersions containing low T_g particles formed homogeneous and transparent films. Experimental evidence suggests that particles deformed under stresses induced by capillary pressure during drying to form films free of voids. Similar experiments with dispersions containing high T_g particles also produced tensile stress but, unlike the film-forming dispersions, the films were opaque and cracked during drying. A model based on the constitutive relation between the stress in a drying film and the imposed strain that also accounts for lateral flow and a spatially varying evaporation rate in a drying film was solved numerically to predict the average bulk stress as a function of time. Comparison of the predicted stresses and the positions of the drying fronts with the measured values for both the film-forming and the non-film-forming dispersions showed an overall good agreement. Deviations were observed, however, in the position of the wet and dry fronts for the films cast from the film-forming dispersions.

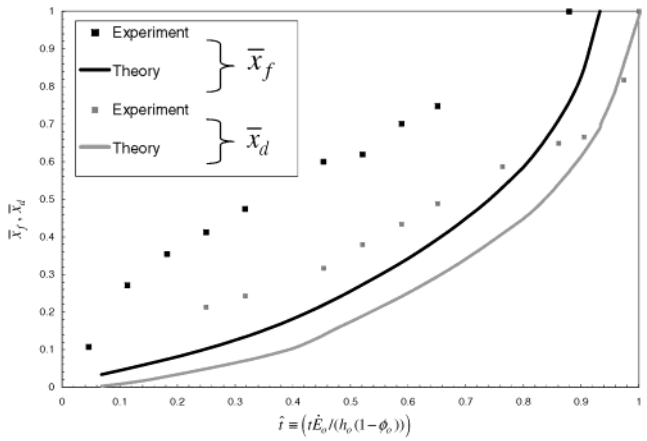

Figure 21. A comparison of the front velocity predicted for case 1 (Table 3) with that measured experimentally for 3 (Table 3). Here, $\bar{x}_d$ and $\bar{x}_f$, are respectively, the positions of the dry and wet fronts.

Acknowledgment. The work reported here was supported in part by the Petroleum Research Fund and the National Science Foundation (CTS 0120421). The authors thank Dr. W. C. Flood of Rohm & Haas and Dr. K. Takamura of BASF for their generous donations of latices. M.S.T. is in debt to Subramanian Ramakrishnan and William Ristenpart for numerous discussions on drying.

LA0356250